University of Groningen

The Sloan Lens ACS Survey. XI. Beyond Hubble Resolution

Newton, Elisabeth R.; Marshall, Philip J.; Treu, Tommaso; Auger, Matthew W.; Gavazzi, Raphaeel; Bolton, Adam S.; Koopmans, Leon V. E.; Moustakas, Leonidas A.

IMPORTANT NOTE: You are advised to consult the publisher's version (publisher's PDF) if you wish to cite from it. Please check the document version below.

Document Version
Publisher's PDF, also known as Version of record

Publication date:
2011

[Link to publication in University of Groningen/UMCG research database](#)

THE SLOAN LENS ACS SURVEY. XI. BEYOND HUBBLE RESOLUTION: SIZE, LUMINOSITY, AND STELLAR MASS OF COMPACT LENSED GALAXIES AT INTERMEDIATE REDSHIFT

Elisabeth R. Newton[1], Philip J. Marshall[1,2], Tommaso Treu[1,7], Matthew W. Auger[1], Raphaël Gavazzi[3],
Adam S. Bolton[4], Léon V. E. Koopmans[5], and Leonidas A. Moustakas[6]

[1] Department of Physics, University of California, Santa Barbara, CA 93106, USA; enewton@cfa.harvard.edu
[2] Kavli Institute for Particle Astrophysics and Cosmology, Stanford University, P.O. Box 20450, MS29, Stanford, CA 94309, USA
[3] Institut dAstrophysique de Paris, UMR7095 CNRS, Univ. Pierre et Marie Curie, 98bis Bvd Arago, F-75014 Paris, France
[4] Department of Physics and Astronomy, University of Utah, Salt Lake City, UT 84112, USA
[5] Kapteyn Astronomical Institute, University of Groningen, P.O. Box 800, 9700AV Groningen, The Netherlands
[6] Jet Propulsion Laboratory, California Institute of Technology, 4800 Oak Grove Drive, M/S 169-237, Pasadena, CA 91109, USA

ABSTRACT

We exploit the strong lensing effect to explore the properties of intrinsically faint and compact galaxies at intermediate redshift ($z_s \simeq 0.4$–0.8) at the highest possible resolution at optical wavelengths. Our sample consists of 46 strongly lensed emission line galaxies (ELGs) discovered by the Sloan Lens ACS Survey (SLACS). The galaxies have been imaged at high resolution with the *Hubble Space Telescope* (*HST*) in three bands (V_{HST}, I_{814}, and H_{160}), allowing us to infer their size, luminosity, and stellar mass using stellar population synthesis models. Lens modeling is performed using a new fast and robust code, KLENS, which we test extensively on real and synthetic non-lensed galaxies, and also on simulated galaxies multiply imaged by SLACS-like galaxy-scale lenses. Our tests show that our measurements of galaxy size, flux, and Sérsic index are robust and accurate, even for objects intrinsically smaller than the *HST* point-spread function. The median magnification is 8.8, with a long tail that extends to magnifications above 40. Modeling the SLACS sources reveals a population of galaxies with colors and Sérsic indices (median $n \sim 1$) consistent with the galaxies detected with *HST* in the Galaxy Evolution from Morphology and SEDs (GEMS) and Hubble Ultra Deep Field (HUDF) surveys, but that are (typically) ~ 2 mag fainter and ~ 5 times smaller in apparent size than GEMS and ~ 4 mag brighter than but similar in size to HUDF. The size–stellar-mass and size–luminosity relations for the SLACS sources are offset to smaller sizes with respect to both comparison samples. The closest analog are ultracompact ELGs identified by *HST* grism surveys. The lowest mass galaxies in our sample are comparable to the brightest Milky Way satellites in stellar mass ($10^7 \, M_\odot$) and have well-determined half-light radii of $0\rlap{.}''05$ (≈ 0.3 kpc).

Key words: galaxies: evolution – galaxies: fundamental parameters – gravitational lensing: strong

Online-only material: color figures

1. INTRODUCTION

Understanding how galaxies were formed and how they evolve into those we see today is an important cosmological question. In hierarchical galaxy formation, gas condenses and cools within a dark matter halo. To form disk galaxies, tidal torques impart angular momentum to the dark matter halo and associated baryons; angular momentum is conserved as the disk galaxy forms within the halo (Fall & Efstathiou 1980). The most massive late-type galaxies are predicted to have formed from mergers of smaller progenitors. However, such models are complicated by the details of star formation, feedback processes, cluster interactions, and effects of the bulge (e.g., Mo et al. 1998).

Models for galaxy formation and evolution predict certain relations between the basic physical properties of galaxies (i.e., luminosity, size, and mass); quantifying these relations can help test the standard paradigm of galaxy formation and place limits on future models. The size–magnitude (or luminosity) and size–mass relations are well studied locally (e.g., Shen et al. 2003; Driver et al. 2005). The relations for early- and late-type galaxies (typically defined as having Sérsic index $n > 2.5$ or <2.5) are found to diverge.

Shen et al. (2003) looked at the mass–size and size–magnitude relations for galaxies in the Sloan Digital Sky Survey (SDSS). A characteristic mass of $M_* = 10^{10.6} \, M_\odot$ delineates two regimes for the SDSS size–mass relation: above this mass, the relation is steeper and tighter (r_{eff} (kpc) $\propto M_*^{0.39}$, $\sigma_{\ln R} = 0.34$ dex) than for less massive galaxies (with r_{eff} (kpc) $\propto M_*^{0.14}$, $\sigma_{\ln R} = 0.47$ dex). The behavior of the size–magnitude relation is similar.

Surveys of intermediate ($0.1 < z < 1$) and high ($z > 1$) redshift galaxies have attempted to extend studies of the size–mass and size–magnitude relations (e.g., Ferguson et al. 2004; Barden et al. 2005; McIntosh et al. 2005; Trujillo et al. 2006; Melbourne et al. 2007). The Galaxy Evolution from Morphology and SEDs (GEMS), a *Hubble Space Telescope* (*HST*) survey, allowed Barden et al. (2005) to study the magnitude-size and mass–size relations of late-type galaxies out to $z \sim 1$. They found a dimming of ~ 1 mag from this redshift to $z = 0$ in the rest-frame *V* band, but noted that the mass–size relation stays constant. Using the Hubble Deep Field South, Trujillo et al. (2006) extended the SDSS and GEMS work out to $z \sim 2.5$, for the most luminous and massive galaxies. The authors find that for low Sérsic indices, galaxies at a given luminosity were $\sim 3.0 \pm 0.5$ times smaller at $z \sim 2.5$, while galaxies at a given mass were $\sim 2.0 \pm 0.5$ times smaller.

Melbourne et al. (2007) inferred the size–magnitude relation for blue galaxies in the Great Observatories Origins Deep

---

[7] David and Lucille Packard Research Fellow.

Survey (GOODS; Giavalisco et al. 2004). These authors found $\sim$1.6 mag of dimming in the B band since $z \sim 1$ for large- and intermediate-sized galaxies ($r_{\rm eff} > 3$ kpc), in agreement with GEMS. Small galaxies, on the other hand, were found to have dimmed significantly more, by some 2.55 ± 0.38 mag in B; this significant evolution is hypothesized to be the result of the fading of the starburst galaxies rather than strong evolution of the entire small galaxy sample.

These studies are limited by the resolution and completeness of the *HST* surveys: for GEMS, these limits correspond to galaxies with $M_* > 10^{10}\,M_\odot$ and $M_V < -20$, as determined by the highest redshift bin ($z \sim 1$). Meanwhile, Trujillo et al. (2006) could only look at galaxies with $L_V > 3.4 \times 10^{10}\,h^{-2}\,L_\odot$ and stellar mass $M_* > 3 \times 10^{10}\,h^{-2}\,M_\odot$.

One method of reaching to lower luminosities is to use exceptionally long exposure times: the Hubble Ultra Deep Field (HUDF; Beckwith et al. 2006) is the prime example of this. Much of the work on the HUDF has been centered around high-redshift galaxies ($z > 1$), but several authors have looked at the low-redshift sample. This sample is primarily comprised of faint objects, since the field was directed away from nearby bright galaxies. Coe et al. (2006) observe large numbers of faint blue galaxies with magnitudes as low as $M_B = -14$ at $z = 0.7$—believed to be young starburst galaxies—which peak at $z \sim 0.67$. Two additional spectral energy distribution (SED) templates with a steep rise toward bluer wavelengths were added to accommodate these objects. Cameron & Driver (2007) look at the size–luminosity relation for HUDF galaxies with $0.2 < z < 1.15$. The best-fit evolution scenario is one with a brightening of 0.9 mag and a 5% decrease in size from $z \sim 0.1$ to $z = 0.675$. This is consistent with the 1 mag arcsec^{-2} of dimming since $z \sim 1$ found in other surveys.

Gravitational lensing is another method of extending surveys to potentially smaller, fainter, and less massive galaxies and does not rely on extremely deep imaging. In strong lensing, a massive foreground galaxy deflects the light from a background object, resulting in multiple images of the source being seen. The source, in addition to being distorted, is typically magnified by a factor of $\sim$10. This phenomenon allows the study of objects smaller than otherwise possible: the tiny source galaxy of gravitational lens J0737 + 3216 was studied by Marshall et al. (2007), while Stark et al. (2008) and Swinbank et al. (2009), for example, have used lenses to carry out detailed studies of high-redshift galaxies.

In this paper, we study a sample of gravitationally lensed galaxies, selected from the Sloan Lens ACS Survey (SLACS; Bolton et al. 2008; Auger et al. 2009, hereafter Paper V and Paper IX). These objects were previously modeled in the F814W filter; here, we perform multi-filter modeling, which allows us to reconstruct the source galaxy SED, and hence infer its stellar mass. Our aim is to investigate the size–mass and size–magnitude relations for these galaxies, and thus explore the potential of gravitationally lensed galaxies to further the study of galaxy formation and evolution.

This work is organized as follows. We introduce our lens sample in Section 2, then give our multi-filter source and lens models for the SLACS sources in Section 3. We discuss the properties of the lensed sources and make a comparison to the GEMS and HUDF samples in Section 4. In Section 4.5, we compare our galaxies to those found in recent emission line surveys. We discuss and summarize our results in Section 5. A discussion of our new lens-modeling code, designed to perform fast and robust lens modeling on large numbers of images, is

reserved for the Appendix; we also present tests on simulated gravitational lenses and on both real and simulated non-lensed galaxies here.

Throughout, we assume a flat ΛCDM cosmology with $h = H_0/(100\ {\rm km\ s^{-1}}) = 0.7$ and $\Omega_{\rm m} = 0.3$. Apparent magnitudes are given in the AB system unless otherwise stated, while Johnson V- and B-band absolute magnitudes are given in the Vega system. All sizes are effective radii, and we follow Peng et al. (2002) and Barden et al. (2005) and define them on the major axis: for an elliptically symmetric surface brightness distribution, the elliptical isophote containing half of the total flux has the major axis $r_{\rm eff}$ and subtends area $\pi q r_{\rm eff}^2$, where q is the ellipse axis ratio.

2. THE SLACS LENS SAMPLE

Here we introduce our sample, a set of galaxies at redshift $z_{\rm s} \simeq 0.4$–0.8 being multiply imaged by massive galaxies lying at $z_{\rm d} \simeq 0.2$.

2.1. Sample Selection

We use a subset of lenses from the SLACS survey (Bolton et al. 2008) as our sample. We select those lenses which were classified as "definitely a lens" and were imaged in the V_{HST}, I_{814}, and H_{160} bands. The instruments and filters these refer to are as follows: for the V_{HST}-band, ACS/WFC F555W or WFPC2 F606W, for the I_{814}-band, ACS/WFC or WFPC2 F814W, and for the H_{160}-band, NICMOS/NIC2 F160W. For the majority of the observations a full orbit's exposure ($t_{\rm exp} \sim 2000$ s) is available, except for 15 lenses that have only *HST* Snapshot images in ACS/WFC F814W ($t_{\rm exp} = 420$ s). For details on the observations and data analysis, as well as full object coordinates, see Paper IX. All images were drizzled onto a pixel scale of 0$\farcs$05. This multi-filter sample comprises 46 lensed galaxies.

2.2. Subtraction of Lens Galaxy Light

When performing lens modeling, we attempt to fit the often-faint lensed images, which can be hidden by or confused with light from the lens (foreground) galaxy; thus, it is necessary to remove the light of the lens galaxy prior to modeling. As the SLACS survey preferentially selects bright lens galaxies this is particularly important for our work. We use the radial B-spline technique, first introduced by Bolton et al. (2006, in the appendix), for this purpose. We refer the reader to Paper V for a full discussion of this method, but provide a brief summary here. First, zero-weight pixels, neighboring objects, and potential source galaxy features are masked. Second, the data are fit using only monopole, dipole, and quadrupole terms in the angular structure. The lensed features are masked based on the residual image from this initial fit; the image is then re-fitted using higher order multipole terms as necessary. Marshall et al. (2007) estimated that the systematic errors in the source size and brightness due to the subtraction of lens galaxy light by this method are approximately 2% (0.01 kpc for a 0.6 kpc source at $z_{\rm s} = 0.6$) and 0.10 mag, respectively. This is an important but usually not dominant source of systematic error. Similarly, subtraction of the lens galaxy may introduce a systematic uncertainty on the Sérsic index, similar to those introduced by improper sky subtraction; based on the detailed work by Marshall et al. (2007), we estimate this systematic uncertainty to be of order 0.1–0.2. This is larger than random errors, but does not effect the results of this paper.

3. THE SLACS SAMPLE: MASS MODELS AND MEASUREMENTS OF SOURCE OBSERVABLES

In the Appendix, we demonstrate our ability to measure galaxy sizes and magnitudes through galaxy-scale gravitational lenses with KLENS; here we use KLENS to measure the size, magnitude, and Sérsic index of the SLACS sources themselves. We refer the interested reader to Paper V and Paper IX for images of the SLACS lenses prior to lens galaxy subtraction and the reconstructed source planes in the F814W filter.

3.1. Models of Lens and Source Galaxies

We have modeled the SLACS lenses in three filters; the data and model lens planes for the primary modeling filter are shown in Figure 1. In order to obtain robust and easy-to-interpret constraints on the source galaxies, we make three fairly standard assumptions, for which we give both a priori justification and a posteriori validation.

Assumption 1. As in the testing program described in the Appendix, we use only one source galaxy, even though in a few cases the source is evidently more complicated (see Bolton et al. 2008). Without this assumption, we would be unable to interpret the size and stellar mass of the galaxy. The alternative would be to use a more complex source model, perhaps defined on a pixelated grid (e.g., Warren & Dye 2003; Treu & Koopmans 2004; Brewer & Lewis 2006; Suyu et al. 2006; Vegetti & Koopmans 2009), and then derive the size and magnitude of the source from this complex model. However, imposing a simple, one-component Sérsic model is standard in the study of faint galaxies, even though they may have irregular morphologies or multiple knots of star formation (e.g., Ferguson et al. 2004). If we are to compare our sample with others in the literature, we need to derive the same parameters as were studied by previous authors. A potential concern is that oversimplification in the source surface brightness distribution may lead to small biases in the mass model. However, as we discuss in Section 3.2, comparison of our mass model parameters with those inferred using complex multicomponent source distributions shows that, at least for the SLACS sources, this is a negligible source of error. In conclusion, considering that using a simple analytic source model greatly speeds up computation time (∼15 minutes in our approach compared with several hours for a typical pixel-based source reconstruction, with a standard desktop CPU), we adopt this procedure.

Assumption 2. We require that the mass model be identical across the different filters, in order not to bias our source reconstruction. Although ideally this would be avoided naturally because there is only one deflector potential, lens galaxy subtraction and differences in contrast and signal-to-noise ratio (S/N) can result in small differences, which we quantify as follows. Using the I_{814} band as reference, we found the difference in σ_{SIE} to be, on average, 0.6 km s^{-1} with an rms scatter of 13.5 km s^{-1} in the H_{160} band, and -2.0 km s^{-1} with an rms scatter of 11.5 km s^{-1} in the V_{HST} band. Likewise, the difference in mass distribution axis ratio q was, on average, -0.007 with an rms scatter of 0.15 in the H_{160} band and -0.03 with an rms scatter of 0.12 in the V_{HST} band. Two or three outliers (defined as having $|\Delta\sigma_{\mathrm{SIE}}| > 50$ km s^{-1} or $|\Delta q| > 0.6$) were excluded from each of these calculations. Fixing the mass model to that of the highest S/N reconstruction ensures that we do not introduce any unnecessary extra scatter in the properties of the source.

Assumption 3. We fix the source morphology parameters (position angle, inclination, size, and Sérsic index) to the best-fit values from the filter with highest S/N. (For two-thirds of galaxies this filter is F814W; for the remainder, only snapshot images were available in F814W and the filter with the highest S/N is F606W. Those objects with only snapshot images in F814W are indicated in Table 1.) This is necessary because the S/N sometimes differs significantly between filters, which can cause low-surface brightness features to be missed and result in overly small sizes and Sérsic indices, which in turn affects the inferred magnitude. This procedure, analogous to the SDSS model magnitudes (Abazajian et al. 2009 and references therein), is effectively equivalent to measuring colors within fixed aperture and is widely adopted in order to obtain robust colors when the S/N varies significantly between filters.

Inferred, unlensed angular sizes and apparent magnitudes for the source galaxies are given in Table 1, along with their lens and source redshifts, and a flag indicating whether the V_{HST} band magnitude refers to WFPC2/F606W or ACS/F555W. We also give the total magnification μ of each system. This quantity varies widely, between 2.4 and 44.3; the median magnification is $8.8^{+6.7}_{-5.1}$, where the error bars correspond to the 16th and 84th percentiles. The lens galaxy properties—mass axis ratio, inclination, and the velocity dispersion—are not presented here, as our concern is with the source galaxies. For a thorough treatment of the SLACS lens galaxies, we refer the reader to Paper V and Paper IX.

3.2. Testing Mass Models: Comparison to Previous Work

The F814W images of the lenses in our sample have been modeled by Bolton et al. (2008) and Auger et al. (2009) using multiple objects in the source plane. This gives us the opportunity to test KLENS' ability to model real lenses and estimate systematic (modeling) errors. Although we cannot compare source models (given the different definitions), we are able to look at the effects of using only one source object on inferred mass model parameters. The lens mass model is described by the mass axis ratio (q), the inclination, the velocity dispersion of the best-fitting singular isothermal ellipsoid (σ_{SIE}), and the mass centroid. We compare mass axis ratios and velocity dispersions and find that they agree to within levels expected from systematic errors: the average offset between our fits and those from Paper V is -0.015 ± 0.002 for q and 2.0 ± 0.2 km s^{-1} for σ_{SIE}. The comparison for velocity dispersion is shown in Figure 2.

We can use the scatter of these relations to estimate total errors, including systematics: we calculate 0.07 for the error on q and 1.78% for the error on σ_{SIE}. These are slightly larger than the errors adopted in Paper V (0.05 on q and 1.0% on σ_{SIE}), as expected because our models are less flexible. As discussed by Marshall et al. (2007) and in the summary at the end of the Appendix, if the potential is not perfectly described by an SIE (e.g., Koopmans et al. 2009; Auger et al. 2010) then additional errors will apply to the source galaxy properties. These are taken into account in the analysis of the source population.

We note that one of the systems, J0737 + 3216, has a published source size, magnitude, and stellar mass (Marshall et al. 2007). Even with a completely different lens modeling code, we find lens parameters, source size, and source Sérsic index for this system that are consistent with those in this previous work, providing further confirmation of the robustness of our
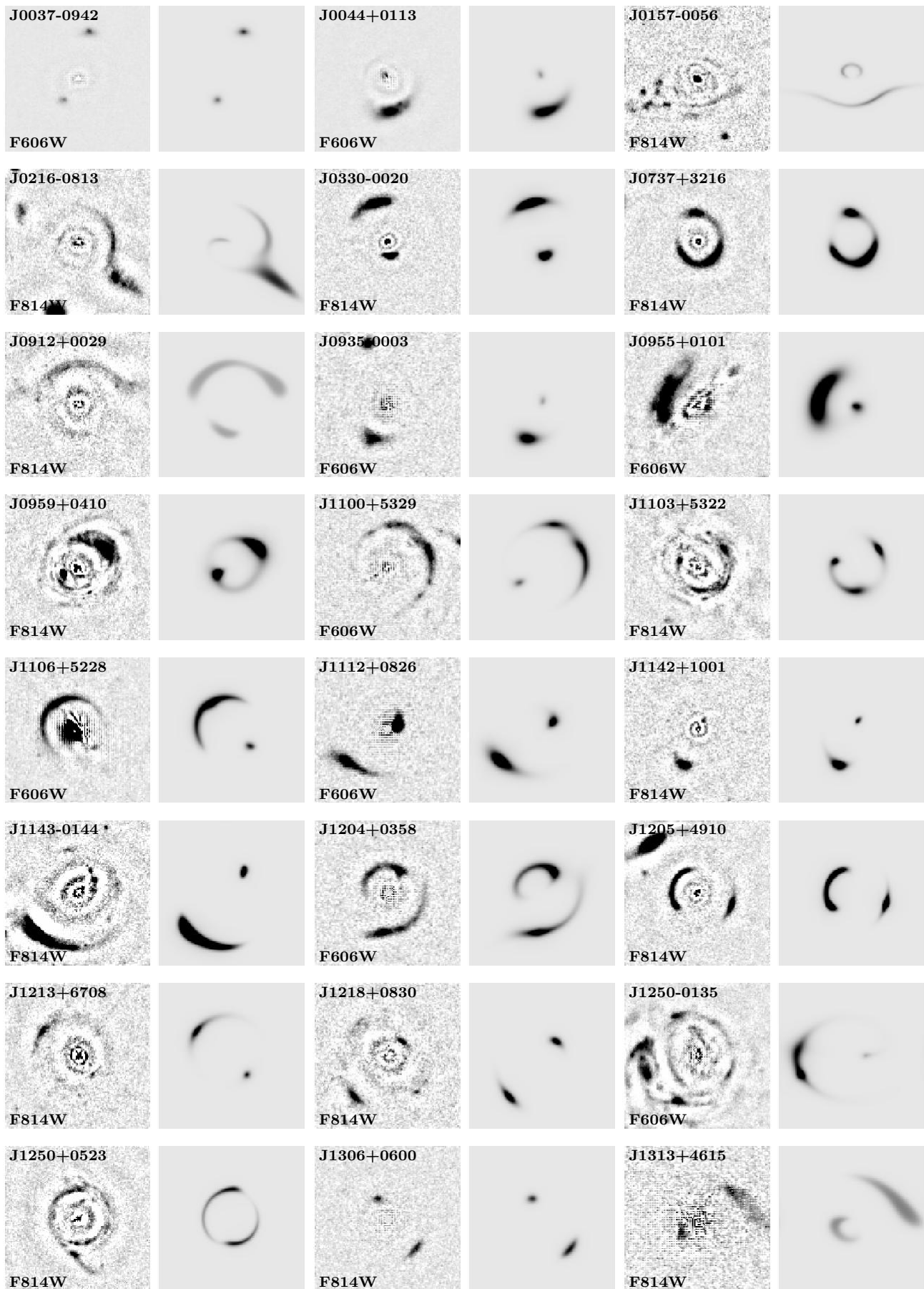
Figure 1. Lens-subtracted *HST* images with KLENS model-predicted arcs. In each case the image in the band with the highest signal-to-noise ratio is shown—this is the image that was used when fitting the lens model. Images are $6'' \times 6''$.
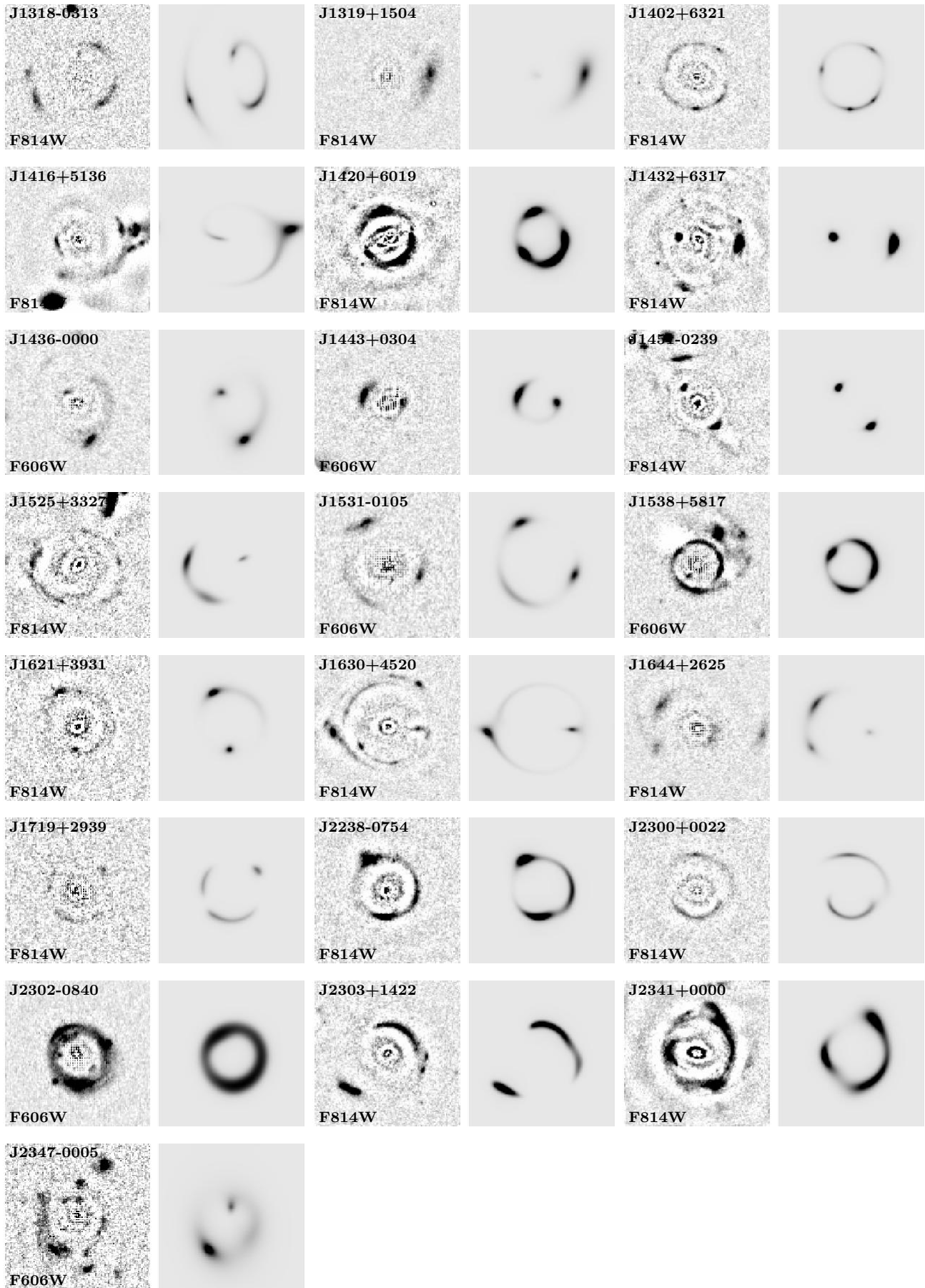
Figure 1. (Continued)

Table 1
Observed Properties of the SLACS Lenses

Name	z_d	z_s	V_{HST}	I_{814}	H_{160}	Instrument	n	r_{eff} (arcsec)	μ
J0037−0942	0.195	0.632	23.96	23.59	23.70	ACS*	1.46	0.06	5.8
J0044+0113	0.120	0.196	21.44	21.05	20.79	ACS*	0.90	0.16	3.6
J0157−0056	0.513	0.924	26.61	25.45	23.16	ACS	1.70	0.83	2.7
J0216−0813	0.332	0.524	24.46	23.25	22.77	ACS	0.33	0.69	3.1
J0330−0020	0.351	1.071	23.46	22.73	22.30	ACS	1.33	0.12	4.0
J0737+3216	0.322	0.581	25.16	24.04	23.62	ACS	1.08	0.11	15.5
J0912+0029	0.164	0.324	25.70	24.92	23.34	ACS	0.20	0.27	10.3
J0935−0003	0.347	0.467	23.91	23.45	22.97	ACS*	0.81	0.16	2.4
J0955+0101	0.111	0.316	22.32	22.44	20.96	ACS*	0.90	0.31	3.1
J0959+0410	0.126	0.535	24.46	22.68	21.36	ACS	2.49	0.08	6.0
J1100+5329	0.317	0.858	25.55	25.42	25.74	ACS*	1.14	0.14	20.6
J1103+5322	0.158	0.735	25.33	24.24	22.45	ACS	1.79	0.11	7.6
J1106+5228	0.095	0.407	25.01	24.60	23.66	ACS*	0.20	0.11	28.0
J1112+0826	0.273	0.630	23.32	23.25	23.14	ACS*	1.54	0.15	3.7
J1142+1001	0.222	0.504	24.74	24.49	24.27	ACS	0.82	0.09	5.2
J1143−0144	0.106	0.402	23.78	23.46	22.43	ACS	0.28	0.15	10.4
J1204+0358	0.164	0.631	24.08	23.70	23.30	ACS*	2.06	0.24	7.9
J1205+4910	0.215	0.481	24.91	24.14	24.63	ACS	1.76	0.06	13.9
J1213+6708	0.123	0.640	25.71	25.42	24.82	ACS	1.99	0.07	10.1
J1218+0830	0.135	0.717	25.08	24.30	23.25	ACS	1.17	0.11	4.2
J1250−0135	0.087	0.353	24.36	23.61	21.90	ACS*	6.15	0.25	13.3
J1250+0523	0.232	0.795	27.01	26.40	23.42	ACS	0.33	0.07	27.9
J1306+0600	0.173	0.472	24.43	24.03	23.96	WFPC2	0.29	0.08	6.5
J1313+4615	0.185	0.514	23.43	22.93	22.04	WFPC2	0.20	0.60	3.2
J1318−0313	0.240	1.300	24.80	23.94	23.46	WFPC2	3.00	0.31	8.4
J1319+1504	0.154	0.606	23.38	22.33	21.41	WFPC2	1.22	0.30	2.6
J1402+6321	0.205	0.481	27.34	26.77	27.30	ACS	3.94	0.10	31.2
J1416+5136	0.299	0.811	24.05	24.21	23.01	ACS	0.94	0.37	5.7
J1420+6019	0.063	0.535	24.68	23.55	22.13	ACS	2.04	0.08	15.9
J1432+6317	0.123	0.664	23.96	23.40	23.26	ACS	0.83	0.06	5.7
J1436−0000	0.285	0.805	24.49	24.11	23.21	ACS*	3.17	0.20	4.8
J1443+0304	0.134	0.419	25.24	25.33	24.99	ACS*	1.04	0.06	8.8
J1451−0239	0.125	0.520	25.68	25.15	24.62	ACS	1.23	0.03	9.1
J1525+3327	0.358	0.717	25.61	25.57	24.16	ACS	0.55	0.15	5.5
J1531−0105	0.160	0.744	25.41	25.26	24.72	ACS*	1.14	0.09	12.4
J1538+5817	0.143	0.531	25.92	26.32	28.96	ACS*	0.49	0.05	44.3
J1621+3931	0.245	0.602	25.15	24.97	24.27	ACS	2.10	0.08	8.8
J1630+4520	0.248	0.793	26.29	25.44	24.67	ACS	1.38	0.21	11.0
J1644+2625	0.137	0.610	24.89	24.66	23.72	WFPC2	2.44	0.11	13.4
J1719+2939	0.181	0.578	27.70	27.00	28.70	WFPC2	0.20	0.05	40.7
J2238−0754	0.137	0.713	25.00	24.17	24.13	ACS	0.94	0.09	15.1
J2300+0022	0.228	0.463	26.56	25.83	25.51	ACS	0.93	0.15	14.0
J2302−0840	0.090	0.222	23.00	24.12	22.27	ACS*	0.28	0.22	13.0
J2303+1422	0.155	0.517	25.13	23.81	23.28	ACS	0.21	0.20	8.0
J2341+0000	0.186	0.807	24.04	23.49	22.13	ACS	0.86	0.21	10.9
J2347−0005	0.417	0.715	24.09	23.96	21.81	ACS*	3.47	0.55	3.2

Notes. AB magnitudes are from the Sérsic model fits in the source plane, and so are unlensed. The effective radius r_{eff} is the major axis of the elliptical isophote containing half the total flux. Uncertainties on r_{eff} and the photometry are 13% and 0.3 mag, respectively. For full coordinates, see Paper IX. A star in the instrument column indicates that only a snapshot was available in I_{814}(F814W).

approach. However, we infer a source that is 1.5 mag fainter uniformly in all bands. This was traced to an error in the modeling code used by Marshall et al. (2007), which summed the flux in twice-subsampled pixels rather than averaging it: this factor of four in flux translates to a magnitude difference of 1.5. After correcting for this "bug" the magnitudes are also in excellent agreement. The results here supercede those published in Marshall et al. (2007).

These comparisons show that our models are reliable and give answers consistent with those obtained by other methods once systematic errors are taken into account.

3.3. Rest-frame Luminosity and Stellar Mass of the Source Galaxies

We now use our multi-band photometry of the SLACS sources to infer rest frame luminosity in the B and V (Johnson Vega) bands as well as stellar masses (M_*). This analysis is based on our models of the unlensed source galaxies, where modeling has been carried out in three separate bands. For this purpose, we use the Bayesian code developed by Auger et al. (2009) to fit stellar population synthesis (SPS) models to our multi-band source galaxy photometry. The code computes, for each
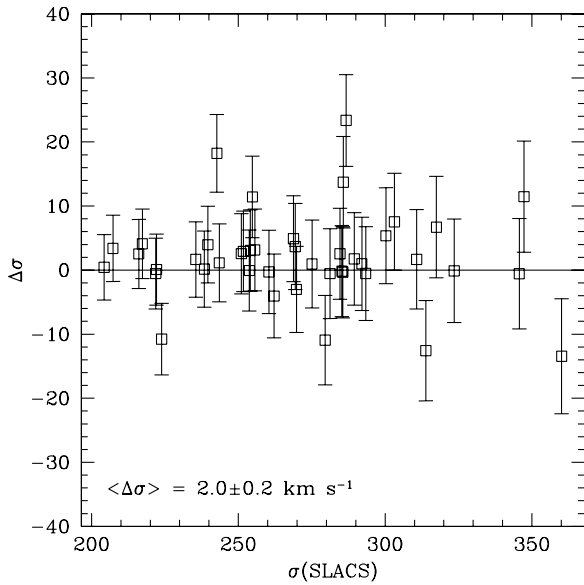
Figure 2. Comparison of best-fit KLENS velocity dispersions to the Paper V or Paper IX value. SLACS values are on the *x*-axis and the difference between KLENS and SLACS is shown on the vertical axis. The average difference is 2.0 ± 0.2 km s^{-1}, and using the rms scatter we estimate the error on σ_{SIE} to be 1.78%. The error bars shown are total errors (2.5%) on the difference.

galaxy, the likelihood of SPS models as a function of stellar mass, age, metallicity, star formation history, and dust content. In combination with a prior on each of these parameters, the likelihood then gives a posterior PDF for each model parameter. The same models and posterior can also be used to generate self-consistent rest-frame luminosities. For this application we adopt SPS models by Bruzual & Charlot (2003) and uniform priors on the logarithm of stellar mass, age, metallicity, and timescale of the exponential star formation history, as is appropriate for the situation where we do not know the order of magnitude of these quantities.

As discussed by Auger et al. (2009 and references therein), although parameters such as age and metallicity are often degenerate, stellar masses and luminosities in the range of wavelength covered by the data can be derived quite accurately for a given initial mass function (IMF). Typical errors on the transformations to rest frame luminosities are of order 0.05–0.1 mag, while typical errors on stellar mass are of order 0.1–0.2 dex (see Table 2 for details). For simplicity we neglect the impact of emission lines on broadband photometry, which is estimated to be of order a few percent for the typical Hα fluxes (the strongest line in the wavelength range of interest) of a few 10^{-16} erg s^{-1} cm^{-2}. Typically, no strong emission line is present in the H_{160}-band filter, which is providing the bulk of the information for stellar mass estimate. The main residual source of uncertainty is the normalization of the IMF. In this paper, we adopt the Kroupa (2001) normalization of the IMF, to facilitate comparisons with the GEMS work (Barden et al. 2005). The uncertainty in the lens mass density profile slope is an additional source of error (Marshall et al. 2007).

As a sanity check we compared our estimated stellar masses with those inferred by applying the "standard" recipe by Bell et al. (2003) to our inferred colors. For the same IMF the stellar masses agree very well, with an average offset of 0.02 ± 0.02 dex (rms scatter 0.15 dex). Our synthetic rest frame photometry agrees well with that inferred by standard "K-correction" procedures (for example, by comparing with the

Table 2
Rest-frame Properties of the SLACS Source Galaxies

Name	B	V	$\log_{10} M_*/M_\odot$
J0037−0942	−18.56	−18.72	$8.61^{+0.12}_{-0.17}$
J0044+0113	−18.02	−18.45	$9.11^{+0.30}_{-0.16}$
J0157−0056	−18.28	−19.07	$9.82^{+0.15}_{-0.17}$
J0216−0813	−18.30	−18.68	$9.13^{+0.17}_{-0.21}$
J0330−0020	−21.00	−21.20	$9.79^{+0.18}_{-0.19}$
J0737+3216	−17.84	−18.19	$8.83^{+0.20}_{-0.18}$
J0912+0029	−15.46	−16.09	$8.65^{+0.15}_{-0.16}$
J0935−0003	−17.93	−18.26	$8.93^{+0.25}_{-0.16}$
J0955+0101	−18.15	−18.70	$9.49^{+0.20}_{-0.15}$
J0959+0410	−18.81	−19.46	$10.03^{+0.18}_{-0.14}$
J1100+5329	−17.51	−17.63	$8.14^{+0.12}_{-0.12}$
J1103+5322	−18.45	−19.20	$9.84^{+0.15}_{-0.17}$
J1106+5228	−16.36	−16.86	$8.72^{+0.23}_{-0.12}$
J1112+0826	−19.10	−19.24	$8.78^{+0.11}_{-0.17}$
J1142+1001	−17.28	−17.44	$8.25^{+0.18}_{-0.17}$
J1143−0144	−17.81	−18.18	$9.00^{+0.23}_{-0.15}$
J1204+0358	−18.57	−18.76	$8.83^{+0.16}_{-0.21}$
J1205+4910	−17.16	−17.30	$8.04^{+0.12}_{-0.16}$
J1213+6708	−16.94	−17.17	$8.25^{+0.16}_{-0.23}$
J1218+0830	−18.23	−18.68	$9.34^{+0.19}_{-0.14}$
J1250−0135	−17.27	−17.96	$9.37^{+0.14}_{-0.15}$
J1250+0523	−16.62	−17.51	$9.46^{+0.15}_{-0.15}$
J1306+0600	−17.39	−17.61	$8.31^{+0.16}_{-0.18}$
J1313+4615	−18.67	−19.12	$9.47^{+0.18}_{-0.18}$
J1318−0313	−20.24	−20.45	$9.51^{+0.13}_{-0.27}$
J1319+1504	−19.58	−20.06	$9.97^{+0.16}_{-0.18}$
J1402+6321	−14.61	−14.73	$6.99^{+0.12}_{-0.13}$
J1416+5136	−19.12	−19.39	$9.29^{+0.22}_{-0.19}$
J1420+6019	−18.19	−18.75	$9.58^{+0.18}_{-0.13}$
J1432+6317	−18.85	−19.07	$8.89^{+0.17}_{-0.19}$
J1436−0000	−18.97	−19.27	$9.29^{+0.22}_{-0.17}$
J1443+0304	−16.09	−16.24	$7.65^{+0.11}_{-0.25}$
J1451−0239	−16.89	−17.08	$8.13^{+0.20}_{-0.15}$
J1525+3327	−17.35	−17.74	$8.89^{+0.21}_{-0.14}$
J1531−0105	−17.81	−17.97	$8.28^{+0.11}_{-0.19}$
J1538+5817	−14.86	−14.97	$7.03^{+0.11}_{-0.12}$
J1621+3931	−17.27	−17.50	$8.46^{+0.18}_{-0.22}$
J1630+4520	−17.36	−17.69	$8.77^{+0.21}_{-0.17}$
J1644+2625	−17.74	−18.06	$8.83^{+0.24}_{-0.16}$
J1719+2939	−14.37	−14.47	$6.86^{+0.11}_{-0.12}$
J2238−0754	−18.27	−18.42	$8.53^{+0.13}_{-0.21}$
J2300+0022	−15.63	−15.89	$7.67^{+0.13}_{-0.23}$
J2302−0840	−16.31	−16.69	$8.28^{+0.21}_{-0.28}$
J2303+1422	−18.03	−18.33	$8.88^{+0.18}_{-0.19}$
J2341+0000	−19.63	−20.08	$9.84^{+0.15}_{-0.17}$
J2347−0005	−19.13	−19.62	$9.89^{+0.16}_{-0.15}$

Notes. Absolute magnitudes are given in the Vega system. Stellar masses were inferred assuming a Kroupa IMF. The typical uncertainty on the absolute magnitudes is 0.17 mag, (0.1 statistical, 0.14 systematic) with an additional 0.26 mag systematic error (which does not affect the color) due to the uncertain lens mass density profile slope. This is also the source of a systematic error of 0.1 dex on the stellar mass, which is included in the given error bars.
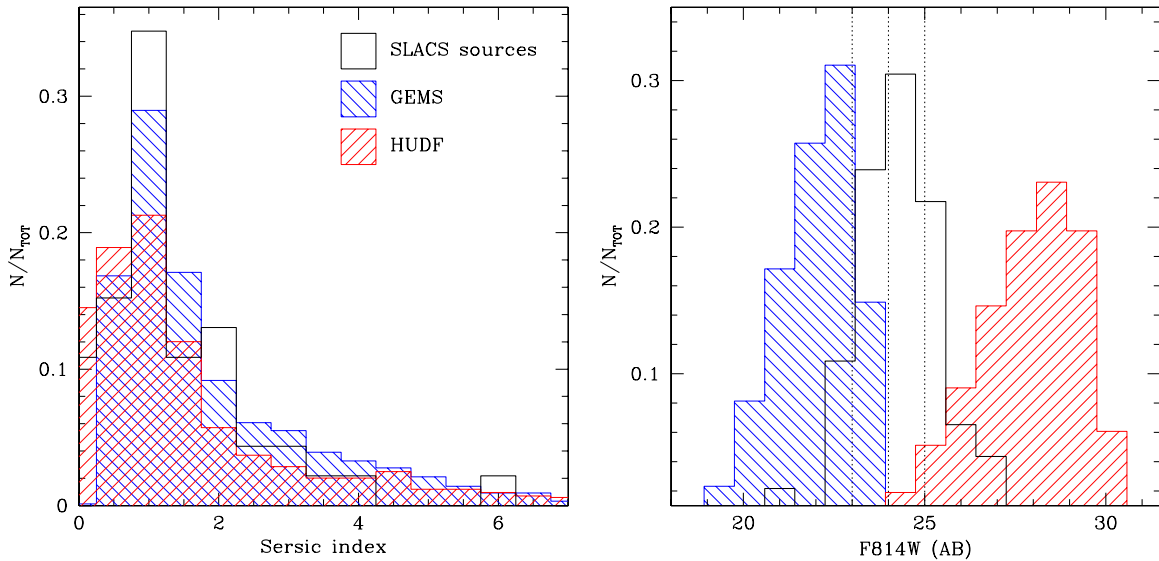
Figure 3. Characteristics of the SLACS lensed sources. The left panel shows the distribution of Sérsic indices for our galaxies (solid unfilled histogram), for GEMS sample with $0.4 < z < 0.8$ (blue, hatched histogram), and for the HUDF sample with $0.4 < z < 0.8$ (red, hatched histogram). The right-hand panel shows the distribution of source apparent magnitudes, corrected for magnification. To compare with the GEMS and HUDF samples we have assumed that F814W=F850LP=F775W (AB), for simplicity. The vertical dashed lines indicate the magnitudes in which KLENS was tested by simulations.

(A color version of this figure is available in the online journal.)

V-band magnitudes inferred via an Sbc template we find an average offset of 0.06 ± 0.06 mag). We conclude that our stellar mass and synthetic photometry are robust and unbiased within the errors.

4. PROPERTIES OF THE SOURCE POPULATION

In this section, we study the properties of the source population. To put our galaxy population in context, we use two comparison samples of non-lensed galaxies observed with *HST* at comparable redshift, by the GEMS and HUDF collaborations. After a brief description of the two samples (Section 4.1), we investigate the distribution of observed properties, i.e., Sérsic index, magnitude, and effective radius (Section 4.3). In Section 4.4, we investigate the bivariate distribution of rest frame quantities, i.e., V-band magnitude, $B - V$ color, effective radius, and stellar mass. Finally, in Section 4.5 we compare the properties of the SLACS sources to those of emission line galaxies (ELGs) selected by blind spectroscopic surveys.

4.1. GEMS-selected Comparison Sample

For the first comparison sample, we follow Barden et al. (2005) and select, from the publicly available GEMS catalog,[8] galaxies with successful GALFIT structural fits (GEMS_FLAG = 4) matched within 0.″5 of a COMBO-17 object with successful photometric redshift estimate (COMBO_FLAG = 3). We did not select galaxies based on their size or Sérsic index (other than to reject objects with large size or Sérsic index uncertainties, or that reached the GALFIT boundary conditions, as did Barden et al. 2005), but we did reject objects not detected in both F606W and F850LP filters. The resulting GEMS sample comprised 6999 galaxies with measured absolute magnitudes and sizes. We adopt the F850LP-measured sizes, since these differ from the rest-frame V-band sizes by typically only 3% (Barden et al. 2005). We then select galaxies in the redshift range $0.4 < z < 0.8$

to approximately match the redshift distribution of SLACS sources, resulting in 3369 galaxies. These are shown as small black points or hatched blue histograms in Figures 3–8. We note that this GEMS subsample represents the brighter part of the GEMS full *HST* catalog with surface photometry, owing to the shallower COMBO-17 multiband photometry used to determine photometric redshifts (completeness limit of $F850LP \sim 23.5$ versus $F850LP \sim 24.5$ for the *HST* catalog; Barden et al. 2005).

We computed stellar masses for all objects in the GEMS sample by applying the recipe by Bell et al. (2003, for a Kroupa IMF) to the rest frame photometry provided in the GEMS catalog. As discussed before, for the SLACS sample the Auger et al. (2009) stellar masses are in excellent agreement with the ones obtained using the recipe by Bell et al. (2003), ensuring that we are able to make this comparison.

4.2. HUDF-selected Comparison Sample

For the second comparison sample, we use the galaxy catalog[9] from the HUDF analyzed by Coe et al. (2006). We selected galaxies in a manner similar to the process used for GEMS. Galaxies included in our sample are those: (1) with good GALFIT fits, (2) that are matched to Beckwith et al. (2003) ACS objects within 0.″5, (3) with successful Bayesian photometric redshifts, and (4) which are detected in B, V, i', and z'. Our criterion for successful GALFIT and redshift fits is that the χ^2 be within 4.5σ of the mean. We also restrict our sample to galaxies in the redshift range $0.4 < z < 0.8$ to match the redshifts of the GEMS and SLACS source samples, for a final tally of 841 galaxies. These are shown as black points or hatched red histograms in Figures 3–8.

We use kcorrect from Blanton & Roweis (2007) to compute rest-frame luminosities of the HUDF comparison sample. We then use the Bell et al. (2003) algorithm to calculate stellar masses, as described in Section 4.1.

[8] The GEMS catalog used in this work can be obtained from http://mpia.de/GEMS/gems_20090526.fits or from M. Barden on request.

[9] The HUDF catalogs used in this work can be obtained from the original paper or from D. Coe at http://adcam.pha.jhu.edu/coe/UDF/.
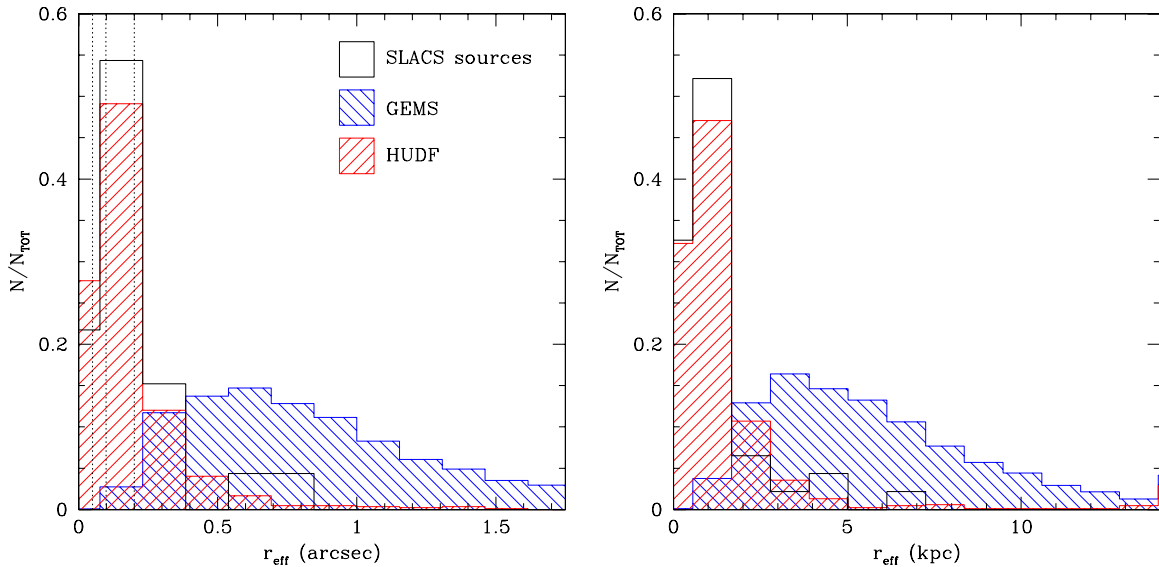
Figure 4. Distribution of source effective radii for our galaxies. The left-hand panel shows sizes in arcseconds; the vertical dotted lines indicate the sizes tested by simulations. The right-hand panel shows sizes in kpc. The SLACS sources sample is shown as solid histograms; the GEMS and HUDF comparison samples are shown as hatched blue and red histograms, respectively.

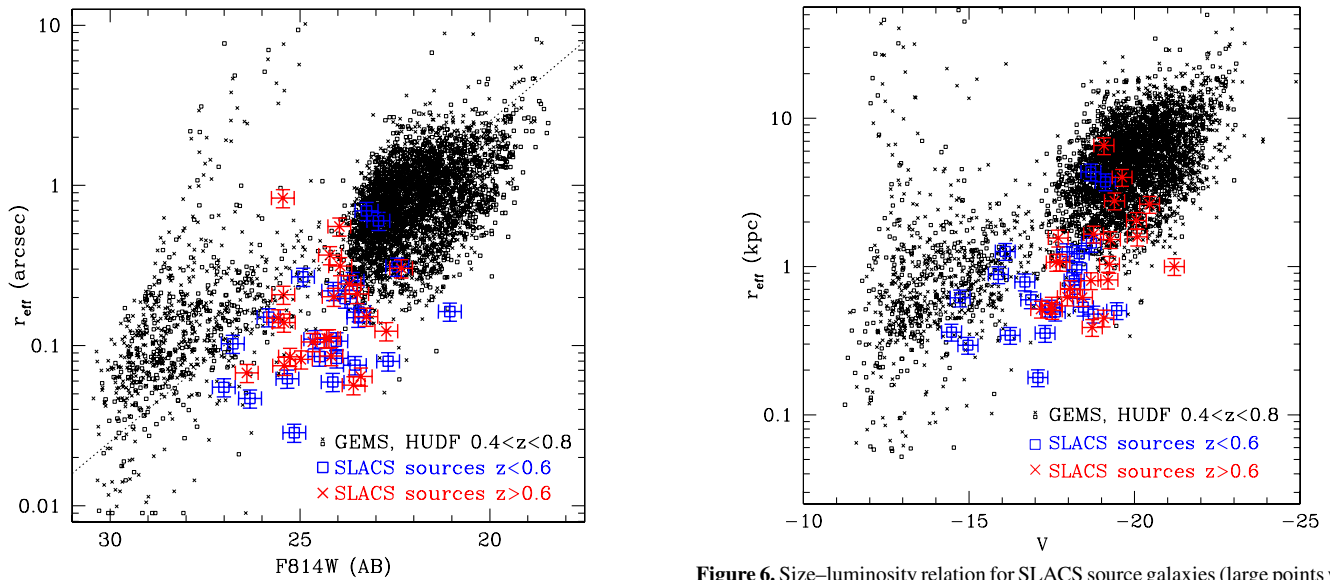(A color version of this figure is available in the online journal.)

Figure 5. Size–magnitude relation for SLACS source galaxies (large points with error bars, with values corrected for magnification) and all GEMS and HUDF galaxies (small points). F814W=F850LP=F775W (AB) has been assumed in the comparison for simplicity. Crosses represent galaxies between $0.4 < z < 0.6$ and squares those between $0.6 < z < 0.8$. The diagonal line represents constant surface brightness of 24 mag arcsec^{-2} in F814W (AB), close to the completeness limit of GEMS for a circular source.

(A color version of this figure is available in the online journal.)

4.3. Distribution of Observed Properties

We plot the distributions of source Sérsic index and apparent F814W source magnitude in Figure 3, showing both the SLACS sources and the GEMS sample. The vertical dotted lines show the magnitudes tested by our simulations, demonstrating that we are in a regime where source properties can be reliably measured by KLENS. In this figure and throughout this work, the quoted source galaxy magnitudes are for the unlensed galaxy, i.e., corrected for magnification.

Figure 6. Size–luminosity relation for SLACS source galaxies (large points with error bars) and all GEMS and HUDF galaxies (small points). Crosses represent galaxies between $0.4 < z < 0.6$ and squares those between $0.6 < z < 0.8$.

(A color version of this figure is available in the online journal.)

When considering apparent magnitudes, the SLACS sources lie squarely between the two regimes sampled by the GEMS and HUDF surveys. Most SLACS source galaxies fall in the range $22 < F814W < 26$, peaking at magnitudes fainter than the completeness limit of the GEMS survey but brighter than most galaxies in the HUDF sample. As mentioned earlier, the drop-off of the GEMS catalog at ~23.5 is mostly due to the COMBO-17 completeness limit. However, a substantial fraction of the SLACS sources are fainter than even the GEMS *HST* completeness limit, suggesting that we are indeed exploring a different population of intrinsically fainter objects. The HUDF survey is much deeper than the SLACS survey (144 *HST* orbits versus one in *I* band), so it is not surprising that these objects are fainter than the SLACS sources. The average magnitudes
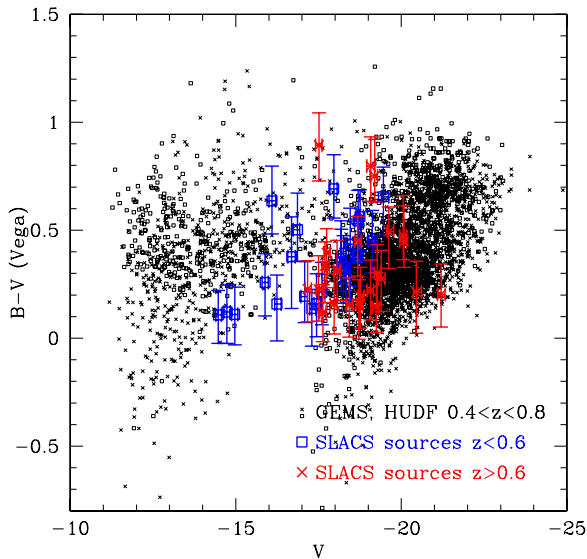
Figure 7. Color–magnitude relation for SLACS source galaxies (large points with error bars) and all GEMS and HUDF galaxies (small points). Crosses represent galaxies between $0.4 < z < 0.6$ and squares those between $0.6 < z < 0.8$. We use rest-frame B- and V-band magnitudes calculated as described in Section 3.3. For our galaxies, we show the rest-frame magnitudes calculated from our stellar mass fitting code.

(A color version of this figure is available in the online journal.)

Figure 8. Size–mass relation for SLACS source galaxies (large points with error bars) and all GEMS and HUDF galaxies (small points). Crosses represent galaxies between $0.4 < z < 0.6$ and squares those between $0.6 < z < 0.8$. Stellar masses for GEMS and HUDF galaxies have been computed using the Bell et al. (2003) recipes. All stellar masses have been converted to a Kroupa IMF normalization.

(A color version of this figure is available in the online journal.)

for the SLACS, GEMS, and HUDF surveys are 24.3, 22.0, and 27.5, respectively.

In contrast, the distribution of Sérsic indices is essentially the same for the three samples—peaked at $n \sim 1$ generally interpreted as dominated by faint disks or compact galaxies—even though the magnitude ranges probed by the three surveys are very different. The median for both SLACS and HUDF is 1.1; for GEMS it is 1.3.

The difference between the SLACS sources and the GEMS galaxies is even more pronounced in terms of the size distribution, shown in Figure 4 with the same notation as Figure 3. The size distribution of GEMS sources is much broader and peaks at 0″.78, petering off below 0″.2. In contrast, Figure 4 highlights the similarity of the SLACS and HUDF galaxies. The overall size distributions for the two samples are remarkably similar, though the HUDF sample extends to much larger sizes, beyond the plotted region. This long tail pushes the average size up to 0″.35 (2.3 kpc) for HUDF, compared to 0″.19 (1.24 kpc) for the SLACS sources. The median sizes, however, are more similar: 0″.12 for HUDF and 0″.14 for SLACS, corresponding to 0.8 kpc for both samples.

The complementarity of the SLACS, GEMS, and HUDF samples is further illustrated by Figure 5 where sizes are plotted against apparent magnitude. With one exception, SLACS sources have comparable surface brightness to that of the GEMS sources, but extend much further down in magnitude and size. A few of the brightest SLACS sources have magnitudes comparable to those of the GEMS sources, but have sizes at the compact end of the distribution. In contrast, the SLACS sources have significantly higher surface brightness on average than the HUDF galaxies.

In Figure 5, crosses represent galaxies in the low-redshift bin ($0.4 < z < 0.6$) while squares indicate the higher redshift galaxies ($0.6 < z < 0.8$). The galaxies in all three samples are not strongly segregated by redshift, consistent with a broad distribution in intrinsic luminosity.
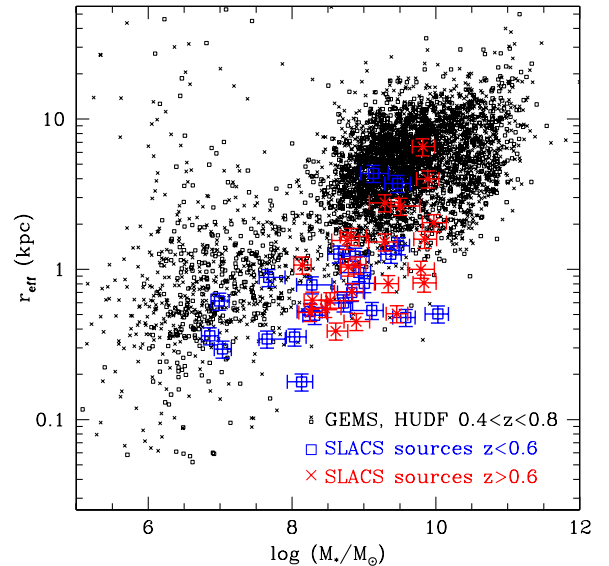
The comparison makes it apparent that the SLACS source population is significantly different from the one studied by typical *HST* broadband imaging surveys such as GEMS. These sources are most likely excluded by *HST* field surveys because they are too faint and/or too compact to be detected and identified as galaxies (as opposed perhaps to stars). Furthermore, even if detected, they are generally too faint and compact to determine their surface brightness profile, size, and stellar mass. The HUDF survey relies on its extremely large exposure times to detect and model such sources. Conversely, SLACS identifies them as galaxies and measures their redshifts via their emission lines (even though they are detected in all three broad bands), and therefore their intrinsic faintness and compactness does not represent an obstacle to detection, while magnification helps in determining their structural parameters. In fact, the distribution of SLACS sources and sizes is in agreement with a generic feature of lensing survey. Owing to magnification bias, faint and compact sources tend to dominate the source population when their number density decreases sharply with luminosity and size (e.g., Treu 2010 and references therein). We will return briefly to the lensing selection function in the next section.

4.4. Distribution of Rest-frame Quantities

We now explore the distribution in size, luminosity, color, and stellar mass for the SLACS source galaxies. We use two-dimensional plots to examine bivariate distributions in the space of well-known correlations representing physical mechanisms: the size–luminosity relation, the color–magnitude diagram, and the size–stellar-mass relation. Again we use the GEMS and HUDF samples as a comparison.

We begin with the size–luminosity relation in Figure 6. We fit a size–luminosity relation of $\log_{10} r_{\rm eff}$ (kpc) $= -0.12 \times V - 2.25$. However, this result should be interpreted with a care, keeping in mind the small number of objects in our sample and the uncertain selection function. A linear extrapolation of the GEMS size–luminosity relation shows little offset between

the GEMS and HUDF galaxies, but the SLACS sources are offset toward smaller sizes by 0.6 kpc or ~30%. This offset may indicate that there is an extended tail of ultracompact galaxies of which the SLACS sources are a part, similar to the population of compact ELGs (Koo et al. 1995; Phillips et al. 1997; Drozdovsky et al. 2005; Straughn et al. 2009).

We note that, as expected for a flux limited sample, the intrinsically fainter objects are only detected at the lowest redshifts (in Figures 6–8, crosses represent galaxies between $0.4 \lesssim z \lesssim 0.6$ and squares those between $0.6 \lesssim z \lesssim 0.8$). Other than this luminosity segregation, no evolution is apparent within our data set.

The color–magnitude diagram shown in Figure 7 paints a similar picture of the properties of the SLACS sources. They span the range of blue colors typical of star-forming galaxies, and of the GEMS and HUDF samples, even with their different intrinsic luminosities. Again, other than luminosity segregation, no evolution is apparent. Our data (and GEMS) are also consistent with no relation between color and magnitude, in contrast to the sample of HUDF galaxies we have selected for comparison, which do show bluer galaxies at higher redshift. This perhaps surprising result is consistent with those of Pirzkal et al. (2006), who looked at ELGs in the HUDF, with $-14 < M_B < -22$ and rest-frame $B - V$ colors from ~0 to ~1. As we discuss below, the SLACS sources may be best represented as ELGs, which could be the cause of this similarity.

Finally, the offset in size with respect to GEMS and HUDF is pronounced even in the size–stellar-mass plane (Figure 8), where the SLACS sources seem to define a sequence offset to smaller radii by 0.5 kpc or ~30%. This indicates that the offset in the size–luminosity relation is not due to abnormally low mass-to-light ratios but to an intrinsic compactness of the population. For the SLACS sources, we find a size–mass relation of $\log_{10} r_{\rm eff}$ (kpc) $= 0.24 \times \log_{10} M_*/M_\odot - 2.20$, although we again caution the reader as to the small sample size and uncertain selection function.

We note that the stellar masses of the SLACS sources are remarkably low for a population at cosmological distances, extending below $10^8 M_\odot$. Three systems in particular have remarkably low stellar mass: J1538+5817 ($z_{\rm s} = 0.531$, $M_* = 10^{7.03} M_\odot$, $L_V = 10^{7.9} L_\odot$), J1402+6321 ($z_{\rm s} = 0.481$, $M_* = 10^{6.99} M_\odot$, $L_V = 10^{7.8} L_\odot$), J1719+2939 ($z_{\rm s} = 0.578$, $M_* = 10^{6.86} M_\odot$, $L_V = 10^{7.7} L_\odot$).

Their V-band luminosities are just 0.5–0.8 dex higher than those of the brighter Milky Way dwarf satellites, Sagittarius and Fornax, and considerably fainter than the Large Magellanic Cloud ($3 \times 10^9 L_\odot$; van der Marel et al. 2002). As can be seen in Figure 1, these three sources are being lensed into high magnification partial Einstein rings (their total magnifications are the three highest: 44.3, 31.2, and 40.7, respectively). The J1538+5817 source may be a low luminosity satellite of a brighter companion, visible just outside the ring.

4.5. SLACS Sources as Emission Line Galaxies

Although the comparison between our galaxies and GEMS or HUDF is useful—it allows us to compare the physical properties of our galaxies, including stellar mass, to large samples with the same redshift distribution—the selection algorithm for SLACS is quite different from that of GEMS or HUDF. The SLACS sample was selected based on the detection of source galaxy emission lines (Bolton et al. 2004); GEMS and HUDF are both imaging surveys. It is therefore useful to compare the SLACS sample with emission line selected galaxies (ELGs). SLACS is

sensitive to observed fluxes as low as $\sim 6 \times 10^{-17}$ erg s^{-1} cm^{-2} (Bolton et al. 2004; Dobler et al. 2008). Taking into account the effects of magnification the equivalent depth is typically $\sim 7 \times 10^{-18}$ erg s^{-1} cm^{-2}, but can be higher by a factor of a few for the most extreme objects.

ELGs identified by *HST* grism surveys (e.g., Drozdovsky et al. 2005; Straughn et al. 2009) reach comparable depths and provide a good benchmark. Those samples span similar broadband magnitude ranges to the SLACS sources and have comparable sizes. For example, the size distribution of galaxies in the sample of Drozdovsky et al. (2005) is limited to small sizes ($r_{\rm eff} < 0\farcs5$) and peaks at $r_{\rm eff} \sim 0\farcs1$–$0\farcs2$. Magnitudes peak at F814W ~ 24, reaching magnitudes as faint as 27. These are quite similar distributions to those for the SLACS galaxies.

5. DISCUSSION AND CONCLUSIONS

Following an initial foray by Marshall et al. (2007), we have extended the study of the size–mass relation of galaxies to lower masses and smaller sizes by making use of the factor of ~10 magnification provided by the gravitational lenses of the SLACS survey. In order to model this unprecedented sample of 46 gravitational lens systems in three bands (V_{HST}, I_{814}, H_{160}), we have developed and tested KLENS, a new code for fast lens modeling optimized for this work. Extensive testing and comparison with standard codes like GALFIT show that we are able to accurately measure the properties of small, faint lensed galaxies: for a mock lensed galaxy of 25th I_{814}-band magnitude, we are able to recover a $0\farcs05$ size.

The main result of this study is that by exploiting the gravitational lensing effect we have been able to determine sizes and stellar masses of a sample of very faint and compact galaxies, which are typically not studied by imaging surveys and are beyond the reach of normal spectroscopic follow-up. We can derive accurate sizes and stellar masses for SLACS sources that are typically 1–2 mag fainter and 5 times smaller than those of a galaxies selected for structural analysis by typical *HST* imaging survey (GEMS). Although the lensed sources are not as faint as galaxies from extremely deep imaging surveys (HUDF), we are able to reach I_{814} magnitudes of 27 with limited exposure times. For comparison, the HUDF survey is comprised of 400 *HST* orbits, with 144 in *I* band, while the SLACS survey is just one orbit in each band. Furthermore, we identify galaxies that are typically ~30% smaller in effective radius than those identified in the HUDF at comparable luminosity or stellar mass.

The SLACS sources are similar to emission line selected galaxies (e.g., Koo et al. 1995; Phillips et al. 1997; Drozdovsky et al. 2005; Straughn et al. 2009), and as such may represent the building blocks of present-day dwarf spheroidals or perhaps even bulges of galaxies (see Hammer et al. 2001). However, thanks to the lensing effect we can image them at high angular resolution and derive accurate sizes and structural parameters.

The existence of this population highlights the importance of diverse selection criteria for a complete census of the galaxy population. Lensing imposes a completely different selection function than for imaging surveys: in particular, the SLACS sources were selected by their strong, multiple emission lines, which were observed to stand out against the background of an early-type (lens) galaxy spectrum (Bolton et al. 2004). In contrast, the GEMS and HUDF sources were selected on the basis of their broadband flux and morphology, using no information as to their brightness in emission lines. Similarly, it is likely that spectroscopic lens surveys could preferentially select compact galaxies, owing to the larger magnification for

compact sources. Modeling the selection function in detail (for example along the lines suggested by Dobler et al. 2008) is essential to quantify the luminosity function of this population and its abundance relative to the population of broadband selected galaxies and that of emission line selected galaxies. This modeling work goes beyond the scope of this paper but will be pursued in the future with the goal of determining the shape an intrinsic scatter of the size–mass relation taking into account the lensing-selected population.

A brief summary of the main results of this paper follows.

1. Our best-fit lens mass parameters are in good agreement with those found in Paper V and Paper IX in the I_{814} band. To mitigate against the scatter introduced by lens light subtraction in the other, lower S/N filters, we fixed the mass models to those fitted in the highest S/N band.

2. The inferred sources appear to be similar in structure to the galaxies in the GEMS catalog of Barden et al. (2005) and the HUDF catalog of Coe et al. (2006), in the sense that the distributions of Sérsic indices are the same between the three samples. However, the SLACS sources have a significantly different distribution of magnitudes. They are fainter than GEMS, with the peaks of their differential number counts separated by 2 mag, and brighter than HUDF by about 4 mag. (However, SLACS reaches these magnitudes with only one *HST* orbit in *I* band, while HUDF uses 144.) Aside from this shift, the color–magnitude diagrams of the three samples are consistent with each other.

3. The SLACS sources are also significantly smaller than the GEMS galaxies and have sizes similar to the HUDF galaxies. The SLACS sources are made measurable via the lens magnification, while the extremely long exposure time is what allows study of the HUDF galaxies. The size distributions of the SLACS sources and the HUDF galaxies peak at approximately 0.1 arcsec ($\simeq$0.8 kpc); such small, faint objects were likely below the COMBO-17 flux limit used in constructing the GEMS sample or were unresolved in the shallow *HST* images.

4. The closest analog in size and magnitude to the SLACS sources are the faint ELGs identified by blind grism surveys with *HST*.

5. Combining the reconstructed (model) magnitudes from the three *HST* bands, we infer stellar masses for each SLACS source and plot the size–mass relation at $0.4 < z < 0.8$. We then compare to the GEMS and HUDF results, finding that the SLACS sources are offset from the GEMS and HUDF size–mass and size–luminosity relations toward smaller effective radii.

6. Some of our measured objects are very low stellar mass indeed, $\sim 10^7 \, M_\odot$, comparable to the largest dwarf satellites of the Milky Way and fainter than the Large Magellanic Cloud.

This work is a further step toward extending the study of intermediate- and high-redshift galaxies to smaller and fainter galaxies, demonstrating that gravitational lensing can help us probe this regime. A larger sample of lenses will improve the statistical significance; the analysis code we have developed can perform lens modeling simply, quickly, and robustly and will be useful when even large samples of lenses are available. Before this, a fuller understanding of the lensed source selection function will allow us to make a quantitative analysis of the size–mass relation of dwarf galaxies at intermediate redshift and how this relation evolves with cosmic time.

APPENDIX

MEASURING SOURCE GALAXIES WITH KLENS

We aim to measure the magnitude and effective radius of the source galaxies of the gravitational lenses in our sample. In this section we describe a new code, KLENS, designed for fast and robust lens modeling of large number of images (for this paper alone we need to model 138 independent images, i.e., 3 bands for each of the 46 lenses). It is similar in spirit to the software used by Marshall et al. (2007), in that the models for the lens mass and source surface brightness distributions are the same. However, we do not explore the posterior probability distribution (PDF) for the model parameters fully, but instead simply search for the peak of the distribution. This approach saves a considerable amount of CPU time (up to two orders of magnitude), since the computation of the image pixel data likelihood function is relatively expensive—but it gives us only the covariance matrix in the Laplace approximation as opposed to full statistical uncertainties on the parameters. We note however that the error budget in this kind of analysis is totally dominated by systematic errors due to factors such as lens light subtraction, model simplicity, and point-spread function (PSF) approximation (see the following sections and Marshall et al. 2007). Therefore we conclude that, with current CPU limitations, it is more effective to combine minimization with Laplace approximation of the errors with a detailed study of one or more objects to estimate systematic errors (Marshall et al. 2007).

After describing the lens and source models in a bit more detail, we outline our implementation of the prior PDFs and the optimization of the posterior, before demonstrating the code's performance on three test data sets.

A.1. Models

The gravitational lenses in our sample are known to be well approximated by simple, SIE mass distributions (Koopmans et al. 2006). We therefore use an SIE model to describe the mass distribution of the lens galaxy. This model has five parameters: the velocity dispersion σ_{SIE}, elliptical axis ratio $q = b/a$, orientation angle θ_d, and position (x_d, y_d) (see, e.g., Kormann

Table A1
Model Transformations and Hard Limits

Profile	Parameter	Prior	Transformation	Limits
Lens mass profile	Axis ratio $q = b/a$	Uniform	Linear	$[0, 1]$
	Velocity dispersion σ_{SIE} (km s^{-1})	Uniform	Linear	$[150, 400]$
	Orientation angle θ_d (rad)	Uniform	Linear	$[0, \pi]$
	Position x_d, y_d (arcsec)	Gaussian	Error function	$[-1, 1]$
Source surface brightness profile	Position angle (rad)	Uniform	Linear	$[0, \pi]$
	$\cos(i) = q$	Uniform	Linear	$[0, 1]$
	Effective radius r_{eff} (arcsec)	Uniform	Linear	$[10^{-3}, 100]$
	Magnitude m	Power law, index k	Power law, index k	$[10, 30]$
	Sérsic index n	Uniform	Linear	$[0.2, 10]$

et al. 1994, for details). For the source galaxy surface brightness, we use an elliptically symmetric distribution with Sérsic profile. The source model has seven parameters: the position (x_s, y_s), orientation angle θ_s, inclination angle i (more often referred to be $\cos i$, which equals the apparent ellipse axis ratio), effective radius r_{eff}, AB apparent magnitude m, and Sérsic index n. A Sérsic index of $n = 0.5$ corresponds to a Gaussian, $n = 1$ to an exponential disk, and $n = 4$ to a de Vaucouleurs profile (see, e.g., Peng et al. 2002 for details).

In Paper V, we used multiple Sérsic profile components to describe the source galaxy. Because our goal here is to measure the physical properties of the source such as size, magnitude, and mass and compare them with corresponding measurements of non-lensed galaxies in the literature, we choose instead to describe the source as a single object. As a result, we do not expect to be able to fit all our sources to the same level of detail as we did in Paper V. One option would be to remove all lenses with complex sources from our sample; however this would bias us toward smaller and simpler sources, which is undesirable. This same single-component simplification was used in, for example, the GEMS and SDSS size–mass relation studies; restricting ourselves to single-component sources allows us to make direct comparisons with these non-lensing surveys.

Asserting that the assumption of an SIE model for the lens galaxy mass profile is the most significant source of systematic uncertainty, Marshall et al. (2007) estimated the systematic errors in the source size and brightness to be approximately 12% (0.07 kpc for a 0.6 kpc source at $z_s = 0.6$) and 0.26 mag, respectively. However, we note that these errors will be common to all observations of a given lens.

A.2. Priors

To ease the exploration of the model parameter space, we work with hidden parameters constrained to vary uniformly on a hypercube, such that their typical values are around one. These hidden parameters are then transformed to the physical parameters described in the previous section before the predicted image is generated. This transformation need not be linear: in fact, it is used to encode our prior knowledge about the model parameters. For example, a uniform prior PDF is implemented as a linear transformation, while exponentiating a hidden parameter corresponds to assigning a scale-free ("Jeffreys," $1/x$) prior. Truncation of the prior PDFs is achieved where necessary by setting the log likelihood to be very large and negative outside the specified limits. The parameters of our model are listed in Table A1, along with the prior PDFs assigned to them, unit transformation used, and the range over which they are allowed to vary.

A.3. Posterior Evaluation and Optimization

At each point in parameter space visited we compute the pixel value likelihood function. We assume Gaussian errors on the pixel values, given by the weight (inverse variance) map produced during data reduction (Paper IX). The log likelihood is then just minus half the image χ^2. The predicted image, required for this statistic, is computed by mapping each pixel's position back to the source plane via the lens equation, and looking up the value of the model source surface brightness. We oversample the image plane to make sure we resolve the source. The lensed images are then convolved with a model PSF; we use Tiny Tim (Krist 2003) to generate this PSF. Note that we do not model lens galaxy light, only the source surface brightness. We therefore assume perfection subtraction of lens galaxy light, an assumption which incurs the systematic error discussed at the end of Section 2.

Since the prior PDF is implemented by parameter transformation, optimization of the posterior is equivalent to maximizing the log likelihood with respect to the hidden parameters. For this optimization we use the IDL routine MPFIT (Markwardt 2009), which is a generalized implementation of the Levenberg–Marquardt nonlinear least-squares algorithm.

The likelihood function is typically quite sharply peaked, with multiple local maxima to be avoided. We find that a three-step process is required for the global peak to be successfully located. First, we make an initial estimate of the source galaxy parameters using a best-guess mass model: the image pixels are traced through the mass model using the lens equation and flux is accumulated on a grid in the source plane. Where multiple image pixels map to the same source plane pixel, we take their simple average. We then take the initial source galaxy position to be the first moment of this resulting light distribution, while summing all the source plane pixel values provides an initial approximation to the source magnitude (this is usually an overestimate). We gain no knowledge of the source inclination, size, position angle, or Sérsic index in this first stage; the source position and magnitude are the most important for finding a good fit to the data, in the sense that small deviations in these parameters can lead to very low likelihood models.

Next, we refine our initial estimates by running MPFIT, using our initial estimates of the source position and magnitude as its starting point (we initialize the other parameters at typical values). This preliminary run is performed without image plane subsampling, for speed. We also use a deflated weight image (the square root of the weight) in this second stage; this smooths the likelihood function, making it easier for the optimizer to locate the global maximum. Finally, in the third step we re-start MPFIT at the position found in step two to get final maximum posterior model parameters for the mass and source. For this
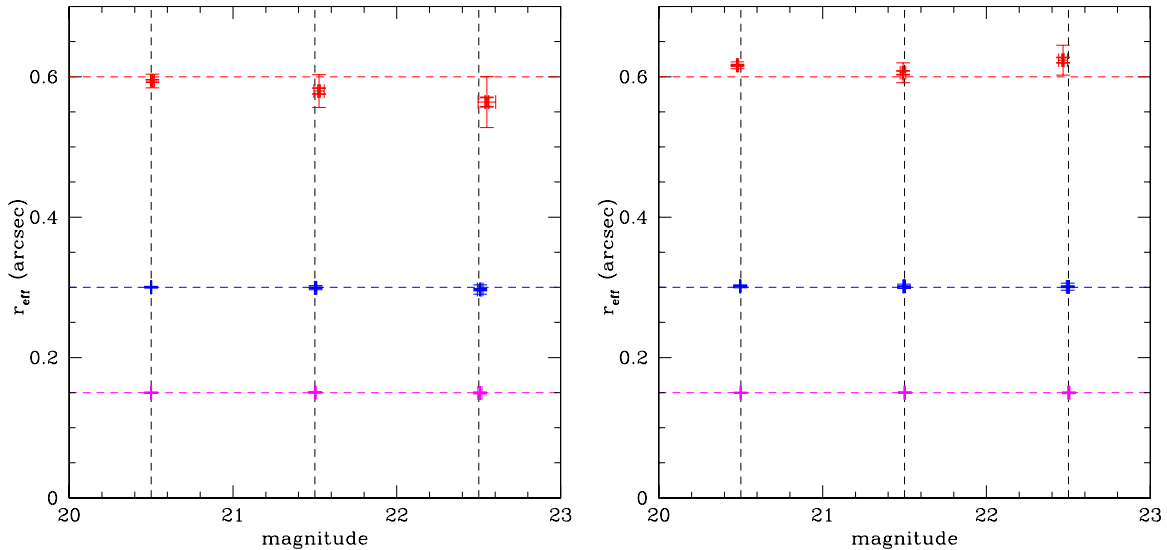
Figure A1. Testing KLENS and GALFIT on simulated non-lensed galaxies. Best-fit effective radii and magnitudes for KLENS (left panel) and GALFIT (right panel), binned by true size and magnitude: the dashed vertical and horizontal lines indicate these bins. Error bars indicate the rms scatter in each bin (the errors on the mean are ~5.5 times smaller and are not shown). In the largest size bins, KLENS tends to underestimate size and overestimate magnitude, while GALFIT tends to do the opposite. (A color version of this figure is available in the online journal.)

final run, we use an image plane oversampling of four (along each axis), and the normal weight image. Convolution with the PSF is done on the oversampled grid; we then use neighborhood averaging to return to the original size.

A.4. Testing KLENS

In order to verify that the KLENS code works properly, we performed tests on (1) simulated non-lensed galaxies, (2) real non-lensed galaxies, and (3) simulated lenses. All simulated data were created using *HST*/ACS I_{814}-band (F814W) image parameters and PSFs, while the real galaxies were selected from *HST*/ACS I_{814}-band images.

A.4.1. Testing KLENS on Simulated Non-lensed Galaxies

We first test KLENS on simulated non-lensed galaxies. Each mock galaxy is taken to be a single elliptically symmetric Sérsic profile component, to allow us to investigate straightforward parameter recovery by the code. The sizes, magnitudes, and Sérsic indices of these galaxies were varied over a 3 by 3 by 3 grid: we chose sizes from $(0\rlap{.}''15, 0\rlap{.}''3, 0\rlap{.}''6)$, magnitudes from $(20.5, 21.5, 22.5)$, and Sérsic indices from $(0.5, 1, 2)$. All position angles were set to $\theta_s = 1.75$ and inclinations at $\cos(i) = q = 0.6$. The simulated galaxies were placed at the center of 42×42 pixel images. Magnified by a typical lens, this size is approximately equivalent to the 122×122 pixel cutouts used for the lenses. We generated ten independent noise realizations for each galaxy, giving a total of 270 simulated observations. The whole sample were then modeled with both KLENS (using the priors given in Table A1) and GALFIT.

The results of the parameter recovery are given in Table A2, which lists the mean (inferred − truth) difference and associated rms scatter values. We look at the results more closely in Figure A1. Overall KLENS and GALFIT give very similar results, although the rms scatter is larger with KLENS. For both modeling programs, the largest galaxies contribute most of the bias, which is in the sense that KLENS tends to slightly underestimate sizes, while GALFIT tends to slightly overestimate them, even though the residual images are consistent with simulated noise. This

Table A2
Mean Parameter Difference (Inferred − True) and Associated rms Scatter for Simulated Non-lensed Galaxies

Parameter	KLENS Models	GALFIT Models
$\langle \Delta m \rangle$	$(118 \pm 1) \times 10^{-4}$	$(-76.0 \pm 0.6) \times 10^{-4}$
σ_m	0.027	0.016
$\langle \Delta r_{\mathrm{eff}} \rangle$	$(-730'' \pm 7) \times 10^{-5}$	$(546'' \pm 4) \times 10^{-5}$
σ_r	0.019	0.012
$\langle \Delta n \rangle$	$(-350 \pm 3) \times 10^{-4}$	$(159 \pm 2) \times 10^{-4}$
σ_n	0.079	0.041

is because the two programs are sampling different parts of the covariance between size, magnitude, and Sérsic index. To illustrate this point, we plot the best-fit Sérsic indices against the best-fit sizes in Figure A2, again grouped by true parameter value.

A.4.2. Test on Real Non-lensed Galaxies

Next, we tested KLENS on real non-lensed galaxies. We selected a sample of 981 galaxies, detected in a subset of the SLACS fields, to match the nine magnitude and size bins used in the previous test: the sample consists of all objects in those fields that have SEXTRACTOR magnitudes $20 < m < 23$ and $0\rlap{.}''1 < r < 0\rlap{.}''65$ that are not stars or image defects. We then ran KLENS on each test image, with the priors given in Table A1; we also ran GALFIT on each data set.

For this sample we do not know the true values for each object's size, magnitude, and Sérsic index; we can only compare GALFIT and KLENS results. When comparing Sérsic indices, we noted significant systematic differences between the two programs, especially at $n > 1.5$. This scatter is, as discussed in Appendix A.4.1, a result of KLENS and GALFIT sampling different parts of the covariance between Sérsic index, size, and magnitude. We compare the two codes' best-fit magnitudes in Figure A3. In this plot we highlight those galaxies for which best-fit Sérsic indices differ by less than 20%; 408 objects meet this requirement. The magnitudes and sizes for these galaxies were found to be in reasonable agreement:
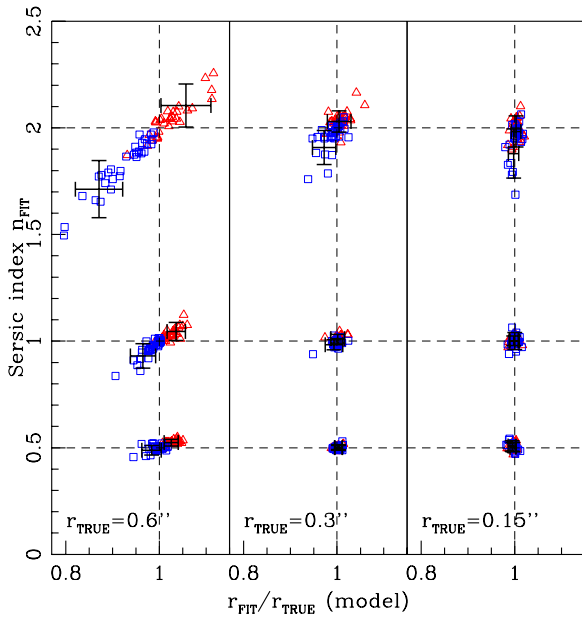
Figure A2. Testing KLENS and GALFIT on simulated non-lensed galaxies. We plot best-fit Sérsic index against the ratio of the best fit to true size, in order to illustrate the covariance between Sérsic index, size, and magnitude. Galaxies are again binned by true Sérsic index and size, shown by the dashed lines. Red triangles indicate GALFIT fits and blue squares indicate KLENS fits. The error bars indicate the mean value and scatter of galaxies in the *faintest* bin (the errors on the mean are ∼3 times smaller and are not shown). The covariance—and the fact that KLENS and GALFIT sample disparate parts of it—is most evident in the $n = 2$, $r = 0\!\!''6$ bin.

(A color version of this figure is available in the online journal.)

$\langle \Delta m \rangle = 0.147 \pm 0.008$ with rms scatter 0.170. A similar analysis for size gives $\langle \Delta r_{\mathrm{eff}} \rangle = -0.174 \pm 0.009$ with rms scatter 0.175. As we decrease the allowable difference in Sérsic index, the bias and scatter both decrease.

GALFIT occasionally returns very low magnitudes relative to the SExtractor values, and that these are associated with Sérsic indices very different from the KLENS values. We note that, for example, Barden et al. (2005) reject objects with GALFIT magnitudes differing from their SExtractor magnitudes by more than 0.6 mag.

A.4.3. Test on a Simulated Lens Sample

Finally, we tested the ability of KLENS to recover the structural parameters of lensed source galaxies. We can do this to a limited extent by comparing our KLENS mass models to the original SLACS lens models (Section 3.2). However, for the source parameters we need to use simulated galaxies, as we did in Section A.4.1 in the non-lensed case. We generated a sample of lensed galaxies to be representative of the possible lensed image configurations and sources. The exact properties of the lens itself are less important: we used the same mass profile ($\sigma_{\mathrm{SIE}} = 270$ km s^{-1}, $q = 0.77$, and $\theta_{\mathrm{d}} = 1.75$ rad, typical parameters for a SLACS lens) for each synthetic system. We also fixed the source galaxy orientation at $\theta_{\mathrm{s}} = 1.75$ rad and its inclination at $\cos(i) = q = 0.6$, again typical values.

The source position, effective radius, magnitude, and Sérsic index were varied, to give 108 possible lenses. We chose four source positions such that the four main lens morphologies (double, caustic, cusp, and quad) were represented. The source effective radius was chosen from ($0\!\!''05$, $0\!\!''1$, $0\!\!''2$), the magnitude from (23, 24, 25), and the Sérsic index from (0.5, 1.0, 2.0). Taking into account magnification due to lensing, these sizes
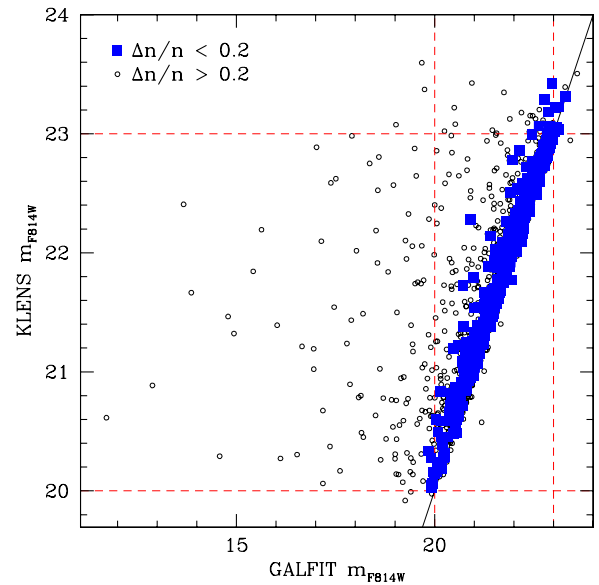

Figure A3. Testing KLENS against GALFIT for real galaxies. Shown are the best-fit magnitudes from GALFIT, on the *x*-axis, and from KLENS, on the *y*-axis. Large filled blue squares are those points for which the percent difference in Sérsic index is less than 20%. The red dashed lines indicate the upper and lower limits on the SExtractor magnitudes for objects in the sample.

(A color version of this figure is available in the online journal.)

Table A3
KLENS Parameter Recovery in a Simulated Lens Sample—Common Lens and Source Parameters

Parameter	True Value	Inferred Value	rms Scatter
q	0.77	0.76044 ± 0.00006	0.063
σ_{SIE} (km s^{-1})	270	269.961 ± 0.007	7.294
θ_{d} (rad)	1.75	1.7368 ± 0.0002	0.221
θ_{s} (rad)	1.75	1.7288 ± 0.0003	0.293
$\cos(i)$	0.6	0.58685 ± 0.00004	0.044

and magnitudes are roughly equivalent to those used in the non-lensed galaxy tests. For each mock system we simulated pixelated images, again with no lens galaxy light. We generated 10 noise realizations for each lens, to give a total of 1080 mock observations. We then ran KLENS on each mock data set, with the priors given in Table A1.

Parameters for which the same true value was used in all simulations (i.e., the lens parameters, and the source inclination and orientation angle) are well modeled, with only small biases well below the rms scatter (see Table A3). We divide the sample into bins to consider the inferences of the remaining parameters, their means and scatters across the sample; these results are presented in Table A4. In Figure A4 we look at the performance of KLENS in recovering the input effective radius and magnitude, binned by their true values.

We find that the inferred parameters are consistent with the input values, albeit with larger scatter than was seen in the non-lensed simulation case. This is partly due to our use of fainter galaxies, which are harder to measure when the image configuration is of lower magnification. (We note that the scatter is smaller for high surface brightness galaxies, indicating that—as might be expected—it is easier to model such galaxies.) It may also be due to the way the information in the data is being used to simultaneously constrain the lens model—to some extent changes in the source parameters can be balanced by changes in the lens model.
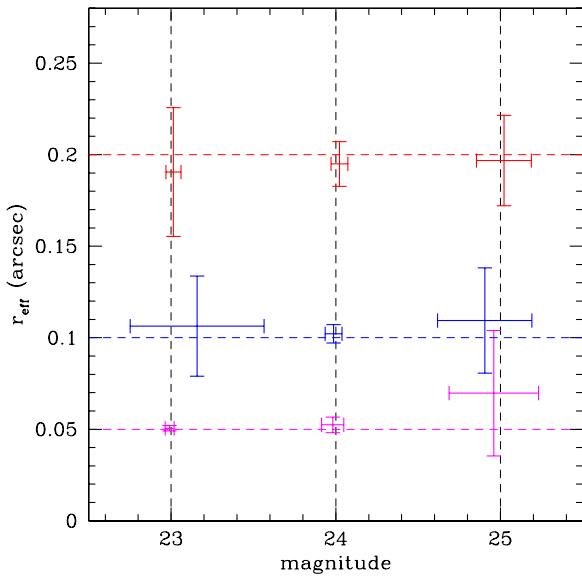
Figure A4. Testing KLENS source parameter recovery on simulated lensed galaxies. We plot KLENS-inferred model magnitude (x-axis) and effective radii (y-axis) for a sample of 1080 simulated lenses. The faint dashed lines again indicate the true parameter values (the nine possible combinations of true size and magnitude occur at their intersections). The data are binned by true size and magnitude; the nine points show the average values for each bin. The error bars again indicate the rms scatter of the inferred parameters (the errors on the mean are 11 times smaller and are not shown).

(A color version of this figure is available in the online journal.)

Table A4
KLENS Parameter Recovery in a Simulated Lens
Sample—Variable Source Parameters

Parameter	True Value	Inferred Value	rms Scatter
Effective radius	$0\farcs05$	$0\farcs0543 \pm 0.0006$	$0\farcs011$
	$0\farcs1$	$0\farcs1023 \pm 0.0009$	$0\farcs016$
	$0\farcs2$	$0\farcs195 \pm 0.001$	$0\farcs022$
Magnitude	23	23.01 ± 0.02	0.107
	24	24.00 ± 0.01	0.062
	25	24.95 ± 0.02	0.265
Sérsic index	0.5	0.62 ± 0.02	0.354
	1.0	1.05 ± 0.01	0.247
	2.0	1.98 ± 0.02	0.291

A.4.4. Summary

We have tested KLENS on three different types of data. Our results on simulated, non-lensed simple Sérsic profile galaxies show that KLENS gives almost identical results to GALFIT; there is a small ($\lesssim 5\%$ for $0\farcs6$ size objects) systematic bias toward larger inferred sizes and Sérsic indices with GALFIT, and a bias of comparable magnitude toward smaller inferred sizes and Sérsic indices with KLENS, as they sample different parts of the covariance. In real, non-lensed galaxies, this covariance results in significant, systematic differences between KLENS and GALFIT inferred parameters, with GALFIT suffering more catastrophic magnitude errors—these have simply been removed in the literature. The difference between the codes is less pronounced if only models with matching Sérsic indices are considered. Finally, testing KLENS on simulated lens systems where the source is a simple Sérsic profile galaxy shows that, for typical expected sizes and magnitudes, KLENS is able to provide accurate measurements of these quantities, with its precision improving with source surface brightness. From this last test (Figure A4),

we estimate that the statistical uncertainties on the source r_{eff} and brightness are 5% and 0.1 mag, respectively. Adding these to the other systematic errors noted above in quadrature, we find overall systematic errors of 13% on r_{eff} and 0.3 mag photometric error (although 0.26 mag in quadrature of the latter—due to assuming an SIE for lens mass model—is common to all filters studied).

REFERENCES

Abazajian, K. N., et al. 2009, ApJS, 182, 543
Auger, M. W., Treu, T., Bolton, A. S., Gavazzi, R., Koopmans, L. V. E., Marshall, P. J., Bundy, K., & Moustakas, L. A. 2009, ApJ, 705, 1099
Auger, M. W., Treu, T., Bolton, A. S., Gavazzi, R., Koopmans, L. V. E., Marshall, P. J., Moustakas, L. A., & Burles, S. 2010, ApJ, 724, 511
Barden, M., et al. 2005, ApJ, 635, 959
Beckwith, S., Somerville, R., & Stiavelli, M. 2003, STScI Newsl., 20, 1
Beckwith, S. V. W., et al. 2006, AJ, 132, 1729
Bell, E. F., McIntosh, D. H., Katz, N., & Weinberg, M. D. 2003, ApJS, 149, 289
Blanton, M. R., & Roweis, S. 2007, AJ, 133, 734
Bolton, A. S., Burles, S., Koopmans, L. V. E., Treu, T., Gavazzi, R., Moustakas, L. A., Wayth, R., & Schlegel, D. J. 2008, ApJ, 682, 964
Bolton, A. S., Burles, S., Koopmans, L. V. E., Treu, T., & Moustakas, L. A. 2006, ApJ, 638, 703
Bolton, A. S., Burles, S., Schlegel, D. J., Eisenstein, D. J., & Brinkmann, J. 2004, AJ, 127, 1860
Brewer, B. J., & Lewis, G. F. 2006, ApJ, 637, 608
Bruzual, G., & Charlot, S. 2003, MNRAS, 344, 1000
Cameron, E., & Driver, S. P. 2007, MNRAS, 377, 523
Coe, D., et al. 2006, AJ, 132, 926
Dobler, G., Keeton, C. R., Bolton, A. S., & Burles, S. 2008, ApJ, 685, 57
Driver, S. P., Liske, J., Cross, N. J. G., De Propris, R., & Allen, P. D. 2005, MNRAS, 360, 81
Drozdovsky, I., Yan, L., Chen, H., Stern, D., Kennicutt, R., Jr., Spinrad, H., & Dawson, S. 2005, AJ, 130, 1324
Fall, S. M., & Efstathiou, G. 1980, MNRAS, 193, 189
Ferguson, H. C., et al. 2004, ApJ, 600, L107
Giavalisco, M., et al. 2004, ApJ, 600, L93
Hammer, F., Gruel, N., Thuan, T. X., Flores, H., & Infante, L. 2001, ApJ, 550, 570
Koo, D. C., Guzman, R., Faber, S. M., Illingworth, G. D., Bershady, M. A., Kron, R. G., & Takamiya, M. 1995, ApJ, 440, L49
Koopmans, L. V. E., Treu, T., Bolton, A. S., Burles, S., & Moustakas, L. A. 2006, ApJ, 649, 599
Koopmans, L. V. E., et al. 2009, ApJ, 703, L51
Kormann, R., Schneider, P., & Bartelmann, M. 1994, A&A, 284, 285
Krist, J. 2003, Inst. Sci. Rep. (Baltimore, MD: STScI), ACS 2003-06
Kroupa, P. 2001, MNRAS, 322, 231
Markwardt, C. B. 2009, in ASP Conf. Ser. 411, Astronomical Data Analysis Software and Systems XVIII, ed. D. A. Bohlender, D. Durand, & P. Dowler (San Francisco, CA: ASP), 251
Marshall, P. J., et al. 2007, ApJ, 671, 1196
McIntosh, D. H., et al. 2005, ApJ, 632, 191
Melbourne, J., Phillips, A. C., Harker, J., Novak, G., Koo, D. C., & Faber, S. M. 2007, ApJ, 660, 81
Mo, H. J., Mao, S., & White, S. D. M. 1998, MNRAS, 295, 319
Peng, C. Y., Ho, L. C., Impey, C. D., & Rix, H.-W. 2002, AJ, 124, 266
Phillips, A. C., Guzman, R., Gallego, J., Koo, D. C., Lowenthal, J. D., Vogt, N. P., Faber, S. M., & Illingworth, G. D. 1997, ApJ, 489, 543
Pirzkal, N., et al. 2006, ApJ, 636, 582
Shen, S., Mo, H. J., White, S. D. M., Blanton, M. R., Kauffmann, G., Voges, W., Brinkmann, J., & Csabai, I. 2003, MNRAS, 343, 978
Stark, D. P., Swinbank, A. M., Ellis, R. S., Dye, S., Smail, I. R., & Richard, J. 2008, Nature, 455, 775
Straughn, A. N., et al. 2009, AJ, 138, 1022
Suyu, S. H., Marshall, P. J., Hobson, M. P., & Blandford, R. D. 2006, MNRAS, 371, 983
Swinbank, A. M., et al. 2009, MNRAS, 400, 1121
Treu, T. 2010, ARA&A, 48, 87
Treu, T., & Koopmans, L. V. E. 2004, ApJ, 611, 739
Trujillo, I., et al. 2006, ApJ, 650, 18
van der Marel, R. P., Alves, D. R., Hardy, E., & Suntzeff, N. B. 2002, AJ, 124, 2639
Vegetti, S., & Koopmans, L. V. E. 2009, MNRAS, 392, 945
Warren, S. J., & Dye, S. 2003, ApJ, 590, 673